

Verification of Design Rules for Mach Zehnder Interferometer

Takeshi Kamijo

Abstract— Integrated photonics are paving the way for a wide range of applications in today's data-driven society. Mach-Zehnder interferometers (MZIs) are key passive photonic components in integrated photonics. Here we report design rules that address the effects of optical path length mismatch and number of waveguide bends on MZI performance. The design rules were validated by comparing experimental data with an introduced transfer function model. The model successfully reproduced the experimental spectrums, and extracted key figures of merit for MZIs, including the effective index, group index and free spectral range. These figures of merit fell within a range predicted by a corner analysis which assessed the manufacturing variability using a waveguide compact model. The validated transfer function model in combination with the corner analysis allow for a robust design framework for MZIs.

Index Terms— MZIs, Transfer function model, Waveguide compact model, Free spectral range.

I. INTRODUCTION

INTEGRATED photonics are paving the way for faster and more efficient data communication in telecoms and data centers, while also enabling emerging a wide range of applications in RF technology, biosensing, LiDAR and quantum computing in today's data-driven society. Integrated photonics enable these applications by manipulating light through the control of amplitude, phase, frequency, and polarization within photonics components. The main components can be categorized into two segments: passive photonic components including waveguides, splitters, fiber grading couplers, ring resonators, and Mach-Zehnder interferometers (MZIs); and active photonic components such as lasers, photodetectors, electro-optic modulators, and optical switches^[1, 2]. The passive photonic components are typically fabricated from silicon (Si) or silicon nitride (SiN) with silicon dioxide (SiO₂) cladding on silicon-on-insulator (SOI) wafer, leveraging advanced and well-established complementary metal-oxide-semiconductor (CMOS) manufacturing processes. Additionally, Si and SiN exhibit high transmission in near-infrared spectrum, particularly at wavelengths of 1550 nm and 1310 nm, which correspond to the C-band and the O-band in optical communication, respectively. Furthermore, Si and SiN cores combined with SiO₂ cladding provide a high refractive index contrast ranging from approx. 0.555 (SiN-SiO₂) to 2.055 (Si-SiO₂), making them ideal for light confinement in waveguides. MZIs, which serve as wavelength-selective optical filters, are one of the most fundamental and widely used passive photonic components in integrated photonics.

Their theoretical principles are well understood. However, in practical photonic devices which integrate multiple components together, the performance of MZIs deviates from theory due to mutual interference in the system and manufacturing variability.

In this report, the transfer function (power transmission efficiency) and free spectral range (FSR) in the quasi-transverse electric (TE) mode are investigated with varying the path length difference and the optical path root structures in MZIs. Additionally, a limited number of identical MZI replicas are implemented to evaluate manufacturing variations across a 605 μm x 410 μm chiplet. Finally, the experimental results are compared with the simulations, discussing deviations between physical numerical models and real devices.

II. THEORY

An MZI controls the selection of constructively interfered light by adjusting the relative phase shift between two beams split light from a single light source. The primary characteristic performances in MZIs are transfer function, *i.e.*, light transmittance spectrum and FSR. In this section, we present the working principles of MZI and derive theoretical equations for their transfer function and FSR to understand design rules of MZIs^[3].

2.1. Working Principles of MZIs

First, the working principles of MZI are introduced. Fig. 1 illustrates a schematic structure of MZIs. MZIs consist of three key components: 1) beam splitters, *e.g.*, Y-branches, directional couplers and multimode interferences (MMIs), 2) two arms which are waveguides to propagate the split lights, and 3) beam combiners which typically utilize the same photonic components as the beam splitters. In this report, a Y-branches are used the beam splitters and combiners. The waveguides of the two arms act as optical phase shifters. When the split optical signals propagating through each arm are in phase, constructive interference occurs at the combiner, ideally resulting in an output light intensity equal to that of the input. Conversely, when the signals are out of phase by 180°, destructive interference takes place, ideally leading to no light at the output. To control the relative phase shift between the two arms, either the refractive indices or the optical path lengths of the arms are varied relative to each other. MZIs are categorized into two types. One is a balanced interferometer two paths of which have equal lengths. The other is an imbalanced interferometer two paths of which

have different lengths. The balanced interferometer modulates the relative phase shift mainly by applying external physical stimuli such as electrical bias, carrier accumulation/plasma dispersion effects (a depletion region controlled by an applied voltage), or thermal effects (a thermos-optic effect) to alter the refractive indices of the arms, thereby functioning as phase shifters. The imbalanced interferometer modulates the relative phase shift by introducing a difference in optical path lengths between two arms, which are composed of identical materials and possess the same refractive index by design.

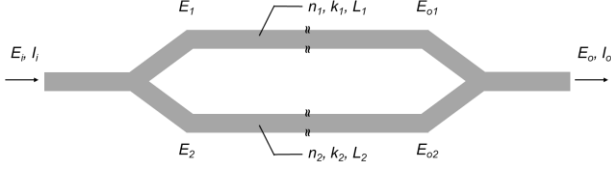


Fig. 1| Top view schematic structure of MZI.

2.2. Transfer Function of Output Light Signal of MZIs

Next, a theoretical equation of transfer function of an output light signal out of MZI is derived. An incoming light signal propagates to the first Y-branch and are split two lights. An ideal Y-branch evenly distributes light intensity between the two arms. An electric field and a light intensity of the split light signal are expressed by the following equation.

$$I_1 = \frac{I_i}{2}, E_1 = \frac{E_i}{\sqrt{2}} \quad (1)$$

$$I_2 = \frac{I_i}{2}, E_2 = \frac{E_i}{\sqrt{2}} \quad (2)$$

where I_i , I_1 and I_2 are a light intensity of one input and two output port, respectively. E_i , E_1 and E_2 are an electric field of one input and two output port, respectively.

The split light signals propagate through two separate waveguides, which may have different refractive indices and different path lengths. A refractive index affects a velocity of light in a medium. Consequently, both parameters contribute to a relative phase shift as the split lights propagate through each arm. Additionally, the lights incur optical loss due to an optical absorption in the waveguides. Here, we consider the propagation of light in a medium with a length of L_1 . The electric field at the beginning of the waveguide ($z = 0$) is expressed as the follow.

$$E_1 = |E_1| \exp(i\omega t) \quad (3)$$

where ω is an angular frequency, and t is time.

The electric field at the output end ($z = L_1$) is given by the following equation by introducing a complex propagation constant of light $\gamma_1 (= \alpha_1 + i\beta_1)$ consisting of an attenuation

constant α_1 ($\alpha_{abs} = 2\alpha_1$, where α_{abs} is an absorption coefficient of light intensity) and phase constant (wave number in the medium) β_1 in the medium.

$$E_{o1} = |E_1| \exp\left(i\left(\omega t - \frac{2\pi(n_1 - ik_1)}{\lambda} L_1\right)\right) \quad (4)$$

$$\alpha_1 = \frac{2\pi k_1}{\lambda} \quad (5)$$

$$\beta_1 = \frac{2\pi n_1}{\lambda} \quad (6)$$

where n_1 and k_1 are a refractive index and attenuation coefficient in the medium, λ is a wavelength of the propagating light.

Substituting eqs. (3), (5), and (6) into eq. (4) leads to the following expression.

$$E_{o1} = E_1 \exp(-i\beta_1 L_1 - \alpha_1 L_1) \quad (7)$$

The light propagating through the other waveguide arm follows the same equation as eq. (7).

$$E_{o2} = E_2 \exp(-i\beta_2 L_2 - \alpha_2 L_2) \quad (8)$$

$$\alpha_2 = \frac{2\pi k_2}{\lambda} \quad (9)$$

$$\beta_2 = \frac{2\pi n_2}{\lambda} \quad (10)$$

Since all other aspects, except for the indices of the variables, are the same as those previously mentioned, the explanation is omitted here.

Eventually, the propagated light signals through the arms are combined in the second Y-branch and create either constructive or destructive interference. An electric field of a light input in one of two waveguides is split equally between the fundamental mode of the waveguide and the higher modes or radiation modes. Therefore, the light at the combiner port output E_o expressed by the following equations.

$$E_o = \frac{E_{o1} + E_{o2}}{\sqrt{2}} \quad (11)$$

Note that an ideal Y-branch combines the light signals out of the arms with substantially negligible power losses.

Finally, An output light signal out of MZIs are the following equations derived by substituting the eqs. (1), (2), (7), and (8) into the eq. (11).

$$E_o = \frac{E_i}{2} \{ \exp(-i\beta_1 L_1 - \alpha_1 L_1) + \exp(-i\beta_2 L_2 - \alpha_2 L_2) \} \quad (12)$$

Therefore, the light intensity at the output port can be expressed by the following equation.

$$I_o = \frac{I_i}{4} | \exp(-i\beta_1 L_1 - \alpha_1 L_1) + \exp(-i\beta_2 L_2 - \alpha_2 L_2) |^2 \quad (13)$$

For the case when the optical loss in the waveguides is 0, eq. (13) is converted to the following equation.

$$I_o = I_i \cos^2 \left(\frac{\beta_1 L_1 - \beta_2 L_2}{2} \right) \quad (14)$$

$$= \frac{I_i}{2} [1 + \cos(\beta_1 L_1 - \beta_2 L_2)]$$

The output interferometer is a sinusoidally varying function of a wavelength and lengths of the waveguides.

For the case of a balanced interferometer, the lengths of the two waveguides are identical. Therefore, eq. (14) is simplified, shown in the following.

$$I_o = \frac{I_i}{2} [1 + \cos(\Delta\beta L)] \quad (15)$$

In this case, a change from constructive to destructive interference is controlled by modulating the refractive index difference between the two waveguides, using effects such as the thermo-optic effect or plasma dispersion. For an imbalanced interferometer, when the materials, more precisely refractive indices of the waveguides are identical but the optical path lengths differ, eq. (14) simplifies to be the following expression.

$$I_o = \frac{I_i}{2} [1 + \cos(\beta\Delta L)] \quad (16)$$

According to the eq. (16), the output light intensity exhibits sinusoidal variations with respect to the optical length mismatch as well as wavelength. Additionally, the period of oscillation is dependent on the optical path length difference. A transfer function of the MZI T_{MZI} is defined as a I_o / I_i . Hence, based on eqs. (13), (15), and (16), the general expression of T_{MZI} , and T_{MZI} for the balanced and imbalanced interferometer can be written by the following equations, respectively.

$$T_{MZI} = \frac{1}{4} |\exp(-i\beta_1 L_1 - \alpha_1 L_1) + \exp(-i\beta_2 L_2 - \alpha_2 L_2)|^2 \quad (17)$$

$$T_{MZI} = \frac{1}{2} [1 + \cos(\Delta\beta L)] \quad (18)$$

$$T_{MZI} = \frac{1}{2} [1 + \cos(\beta\Delta L)] \quad (19)$$

The transfer function is often converted to decibels.

$$T_{MZI, dB} = 10 \log_{10} (T_{MZI}) \quad (20)$$

2.3. FSR of Output Light Signal of MZIs.

Next, a theoretical equation of the FSR of an output light signal from MZI particularly for the case of an imbalanced interferometer is derived. The FSR in wavelength units is the spacing between adjacent peaks of a sinusoidal curve expressed by (19), defined as a the following equation (Fig. 2).

$$\text{FSR} = \Delta\lambda = \lambda_{m+1} - \lambda_m \quad (21)$$

where λ_m and λ_{m+1} are wavelengths of the output light signal at an arbitrary m -th peak and $m+1$ -th peak, respectively.

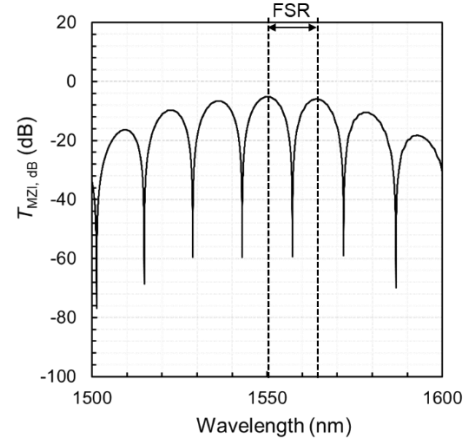


Fig. 2| Representative transfer function of imbalanced MZI. Vertical dotted lines present positions of wavelengths at peaks adjacent to 1550-nm wavelength. FSR is determined by a spacing between adjacent peaks.

An argument of the cosine transfer function is introduced as a δ defined in the following equation.

$$\delta = \beta\Delta L \quad (22)$$

As the phase difference between adjacent peaks is 2π , eq. (22) satisfies the following relation.

$$\begin{aligned} \Delta\delta &= \delta_m - \delta_{m+1} \\ &= \beta_m \Delta L - \beta_{m+1} \Delta L \\ &= 2\pi \end{aligned} \quad (23)$$

where δ_m and δ_{m+1} are phases at the peak wavelengths of λ_m and λ_{m+1} , respectively. In a similar manner, β_m and β_{m+1} are wave numbers at the peak wavelengths of λ_m and λ_{m+1} , respectively. It is noted that a higher order of the interferometer, namely $\delta \gg 2\pi$, is considered here. Therefore, the wave number difference $\Delta\beta$ is converted into the following.

$$\Delta\beta = \beta_m - \beta_{m+1} = \frac{2\pi}{\Delta L} \quad (24)$$

As the wave number is a function of the wavelength, the Taylor expansion of the wave number around λ_m can be applied. When the Taylor series is truncated after the first-order term, neglecting higher-order terms, the wave number difference becomes negatively linearly with respect to the wavelength difference between the adjacent peaks. Therefore, the relation between the wave number difference and the wavelength difference can be written as the following equation.

$$\Delta\beta \approx -\frac{d\beta}{d\lambda} \Delta\lambda \quad (25)$$

Combining eqs. (24) and (25), the wavelength difference is given by the following equation.

$$\Delta\lambda \approx -\frac{2\pi}{\Delta L} \left(\frac{d\beta}{d\lambda} \right)^{-1} \quad (26)$$

From eq. (6), the derivative of the wave number with respect to the wavelength is expressed by the following equation.

$$\begin{aligned} \frac{d\beta}{d\lambda} &= \frac{2\pi}{\lambda} \frac{dn}{d\lambda} + 2\pi n \frac{d}{d\lambda} \left(\frac{1}{\lambda} \right) \\ &= -\frac{2\pi}{\lambda^2} \left(n - \lambda \frac{dn}{d\lambda} \right) \end{aligned} \quad (27)$$

By substituting eq. (27) into eq. (26), the following equation of the FSR is obtained.

$$FSR = \Delta\lambda = \frac{\lambda^2}{\Delta L \left(n - \lambda \frac{dn}{d\lambda} \right)} = \frac{\lambda^2}{\Delta L n_g} \quad (28)$$

where n_g is the group index expressed by

$$n_g = n - \lambda \frac{dn}{d\lambda}. \quad (29)$$

The FSR equation given in (28) demonstrates that the FSR scales quadratically with the wavelength and is inversely proportional to both the optical path length difference and the group index of the propagation light signal in the MZI. The FSR is now converted to a frequency $\Delta\nu$ by the following equation based on $\nu = c/\lambda$.

$$\Delta\nu \approx -\frac{c\Delta\lambda}{\lambda^2} = -\frac{c}{\Delta L n_g} \quad (30)$$

where c is the speed of light. Similarly, the Taylor expansion of the frequency around λ can be performed, truncating the Taylor series after the first-order term, neglecting higher-order terms. In this case, $\Delta\nu$ is a negative value, as we consider the scenario in which the wavelength increases from the reference point λ_m because frequency is inversely proportional to the wavelength. However, the FSR in a unit of Hertz should be a positive value. Therefore, either absolute value of $\Delta\nu$ or $-\Delta\nu$ can be used to represent the FSR.

$$FSR = |\Delta\nu| = \frac{c}{\Delta L n_g} \quad (31)$$

III. MODEL AND SIMULATION

To investigate the effects of path length differences and path root structures on key figures of merit of MZIs, a set of nine imbalanced MZIs was designed, as illustrated in Fig. 3 and detailed in Table 1. The waveguides in all MZIs were identical with a width of 500 nm and a thickness of 220 nm. The bend radius for all waveguides was uniformly set to 5 μm . The primally polarization was quasi-TE mode. The layout design was created using KLayout^[4] in conjunction with SiEPIC-EBEAM-PDK^[5]. Each MZI consisted of two fiber grating couplers and the MZI configuration described in the previous section. The fiber grating couplers were employed to couple light signals between the MZIs and optical fibers connected to a measurement system.

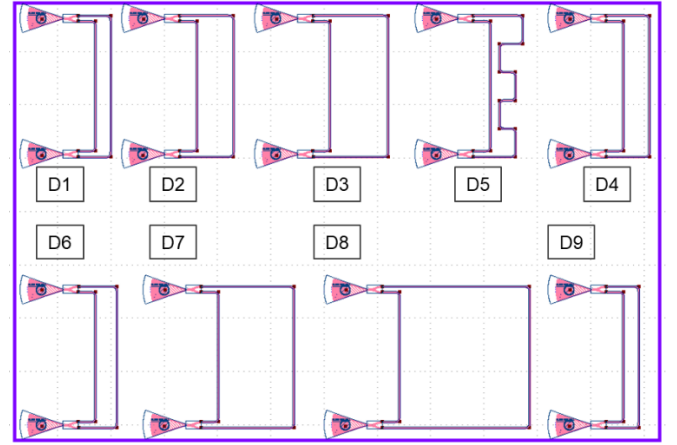


Fig. 3| Layout design of imbalanced MZIs.

In this section, we first introduce the waveguide compact model. Next, the effective index dispersion of a 500 nm \times 220 nm Si strip waveguide with SiO₂ cladding is simulated using Lumerical MODE (Ansys, Inc.). It is fitted using the compact model, computing optical parameters including an effective index, group index and group velocity dispersion. Then, for each MZI shown in Fig. 3, the FSR is calculated using eq. (28) with the obtained group index as an input. Lastly, these figures of merit are compared with simulation results obtained using Lumerical INTERCONNECT (Ansys, Inc.).

3.1. Waveguide Compact Model.

Initially, the waveguide compact model is described^[6]. The effective index n_{eff} varies with wavelength. Therefore, a Taylor expression of n_{eff} with respect to a wavelength around λ_0 can be performed, truncated after the second-order term, neglecting higher-order terms. The obtained second order polynomial is expressed by the following equation.

$$n_{\text{eff}}(\lambda) = n_1 + n_2(\lambda - \lambda_0) + n_3(\lambda - \lambda_0)^2 \quad (32)$$

Eq. (32) can be converted to an effective index n_{eff} , a group index n_g and a group velocity dispersion D at a wavelength of λ_0 , given by the following equations.

$$n_{\text{eff}} = n_1 \quad (33)$$

$$n_g = n_{\text{eff}} - \lambda \frac{dn_{\text{eff}}}{d\lambda} = n_1 - n_2 \cdot \lambda_0 \quad (34)$$

$$D = \frac{1}{c} \frac{dn_g}{d\lambda} = -\frac{\lambda}{c} \frac{d^2 n_{\text{eff}}}{d\lambda^2} = -\frac{2\lambda_0 n_3}{c} \quad (35)$$

Next, a 500 nm \times 220 nm Si strip waveguide with SiO₂ cladding on SOI wafer was modelled, and the effective index dispersion in a range of wavelength from 1500 nm to 1600 nm was computed. Fig. 4 displays the cross-sectional structure of the MZIs studied in this report.

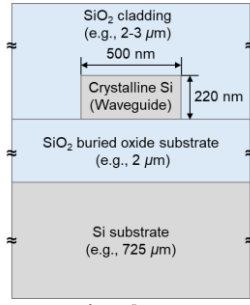


Fig. 4| Schematic cross-sectional structure of a Si strip waveguide with SiO₂ cladding on SOI wafer.

The simulated electric field, magnetic field, and energy intensity of the primary quasi-TE polarization in the waveguide at a wavelength of 1550 nm are displayed in Fig. 5a-c, respectively. This geometrical dimension of waveguide confined a light with this wavelength.

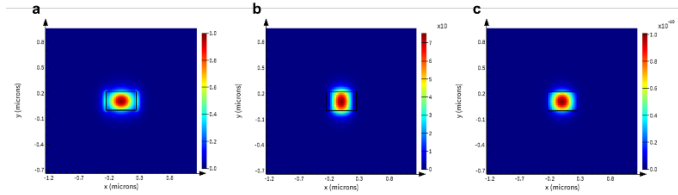


Fig. 5| Simulated light confinement in a Si strip waveguide. a, Electric field, **b,** magnetic field, **c,** optical energy density of a propagating quasi-TE mode at a wavelength of 1550 nm.

Fig. 6 and Fig. 7 present the computed effective index and group index dispersions in a range of wavelength from 1500 nm to 1600 nm, respectively. The effective index was negatively proportional to the wavelength, whereas the group index scaled with the wavelength. Additionally, the fitting curve using the waveguide compact model (eq. (32)) is overlaid. The fitting curve shows good agreement with the simulation results. The coefficient of determination R^2 was 1. The resulted fitting function is expressed by the following.

$$n_{\text{eff}}(\lambda) = 2.443 - 1.132(\lambda - \lambda_0) - 0.040(\lambda - \lambda_0)^2 \quad (36)$$

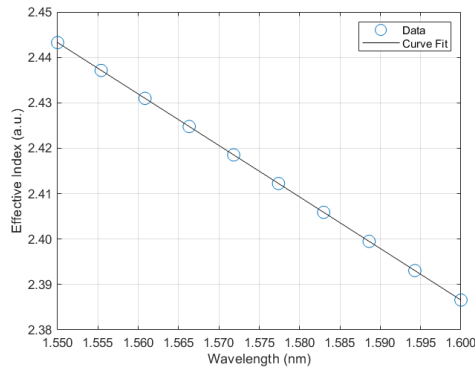


Fig. 6| Fitted curve of waveguide compact model (open blue circle) to simulated effective index profile (black line) as a function of wavelength.

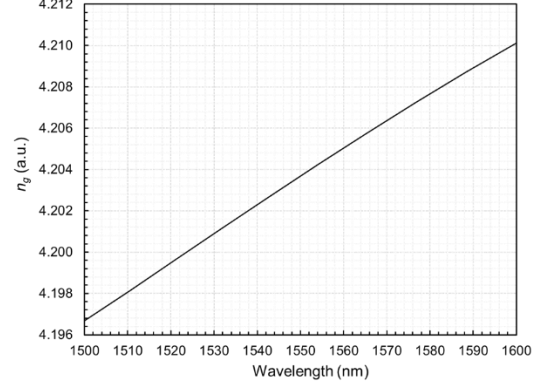


Fig. 7| Simulated group index dispersion.

The derived effective index, group index and a dispersion at a wavelength of 1550 nm using eqs. (33)-(35) are expressed by the following.

$$n_{\text{eff}} = 2.443 \quad (37)$$

$$n_g = 4.197 \quad (38)$$

$$D = 409.9 \text{ (ps/nm/km)} \quad (39)$$

The resulted group index at a wavelength of 1550 nm showed excellent agreement with the computed group index dispersion. The FSR was calculated using the given group index and eq. (28), and is denoted as 'Cal. FSR' in Table 1.

3.2. Simulation results for the designed MZIs

Next, we delve into the design objectives and MZI simulations for each MZIs. The simulated FSR (Sim. FSR) and the group index were compared with calculated results based on the waveguide compact model in Table 1. Starting from MZIs of D1 to D3, those were designed with an optical path length difference ΔL that results in constructive interference near a wavelength of 1550 nm. Based on eq. (19), the optical path length mismatches of D2 and D3 were set to be integer multiples of ΔL relative to D1, specifically 2 times and 3 times, respectively. According to eq. (28), the FSR of D2 and D3 should be half and one-third of that of D1, respectively. The simulated transfer function is depicted in Fig. 8a. The peaks of D1, D2, and D3 near a 1550-nm wavelength were aligned at the same wavelength. The maximum power transmission efficiency near a wavelength of 1550 nm was approx. -5.2 dB. The FSR for each MZI were extracted from the simulated transfer function based on the two nearest peaks around a wavelength of 1550 nm. As per the theoretical formula, the FSR of D2 is half that of D1, and the FSR of D3 is one-third that of D1.

D4 was designed to produce destructive interference near a wavelength of 1550. According to eq. (19), when the path length mismatch is a half-integers multiple of that of D1, the transfer function is expected to exhibit a valley or dip near a wavelength of 1550 nm. Therefore, the path length difference was set to 1.5 times longer than D1.

Table 1| Designs of imbalanced MZIs and comparison between calculated and simulated results.

Device nr.	L_1 (μm)	L_2 (μm)	ΔL (μm)	Cal. FSR ^a (nm)	Sim. FSR ^b (nm)	ΔFSR (nm)	Sim. n_g (a.u.)	Δn_g (a.u.)
D1	150	189.93	39.93	14.34	13.98	-0.35 (-2.5%)	4.304	0.107
D2	150	229.86	79.86	7.17	6.93	-0.24 (-3.3%)	4.340	0.143
D3	150	269.79	119.79	4.78	4.76	-0.01 (-0.3%)	4.210	0.013
D4	150	209.90	59.90	9.56	9.39	-0.16 (-1.7%)	4.271	0.074
D5	150	269.79	119.79	4.78	4.76	-0.01 (-0.3%)	4.210	0.013
D6	150	201.02	51.02	11.22	11.05	-0.17 (-1.5%)	4.261	0.064
D7 (=MZI8)	150	303.06	153.06	3.74	3.76	0.02 (+0.5%)	4.178	-0.019
D8 (=MZI7)	150	405.10	255.10	2.24	2.25	0.01 (+0.1%)	4.193	-0.004
D9	150	189.93	39.93	14.34	13.98	-0.35 (-2.5%)	4.304	0.107

^a Calculated FSR at wavelength of 1550 nm. ^b FSR based on the two nearest peaks around a wavelength of 1550 nm in the MZI transfer function.

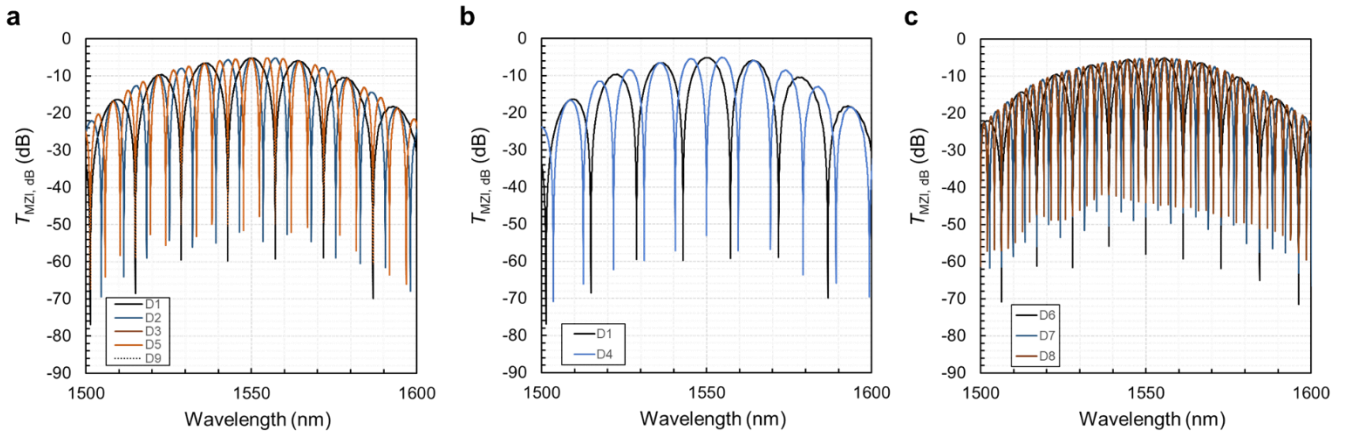


Fig. 8| Simulated transfer functions of designed MZIs. **a**, transfer functions of D1, D2, D3, D5 and D9 in a range of wavelength from 1500 to 1600 nm, resulting in constructive interference at a wavelength of 1550 nm. **b**, transfer functions of D1, and D4 in the same range of wavelength. **c**, transfer functions of D6, D7 and D8 in the same range of wavelength, constructing destructive interference (dips) at a wavelength of 1550 nm.

The simulated transfer function is plotted in Fig. 8b. As per the theoretical formula, the dip in D4 was located near a wavelength of 1550 nm.

Next, D3 and D5 employed the identical optical path length difference but different path root structures. D3 contained two waveguide bends whereas D5 includes ten. The simulated transfer functions are illustrated in Fig. 8a. In the simulations, both transfer functions were identical and completely overlapped, regardless of the different path root structures. Nevertheless, as shown in Fig. 9, which compares light confinement between a straight waveguide and waveguide bend, the total energy loss of D5 is expected to be higher than that of D3. We verified this hypothesis in the experimental section.

Following this, D6, D7, and D8 were designed with an optical path length difference that results in destructive interference near a wavelength of 1550. Using eq. (19), the optical path length mismatches of D7 and D8 were set to be odd multiples of ΔL relative to D6, specifically 3 times and 5 times, respectively. According to eq. (28), the FSR of D7

and D8 are expected to one-third and one-fifth of that of D6, respectively. The simulated transfer function is depicted in Fig. 8c. The dips of D6, D7, and D8 near the 1550-nm wavelength show excellent agreement.

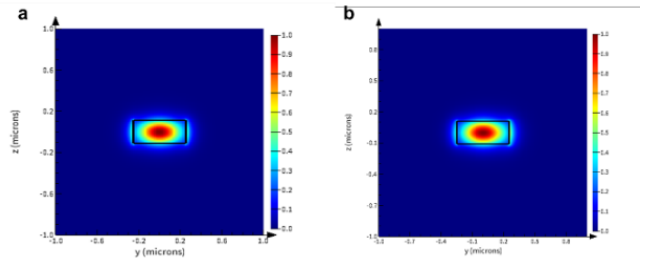


Fig. 9| Electric field distribution in waveguides. **a**, electric field of quasi-TE mode in a 500 nm \times 220 nm straight waveguide. **b**, electric field of quasi-TE mode in a 500 nm \times 220 nm waveguide bend with a bend radius of 5 μm . The electric field in the waveguide bend shifted toward the outer edge of the bend (right side), resulting in an optical power loss of 0.2%

Lastly, to assess manufacturing variability across the 605 μm \times 410 μm chiplet, D9 which had the identical design to D1

was placed diagonally opposite to D1. As shown in Fig. 8a, the transfer function completely overlapped with that of D1. Overall, the obtained FSR showed great agreement with the calculated values, with a deviation of even or less than 3.3% (Table 1). Similarly, the resulting group indices reproduced those derived from the waveguide compact model, with a deviation of 2.5% or less.

IV. FABRICATION

The MZI devices were fabricated using a 100-keV electron beam lithography (EBL) patterning technique as a part of a multi project wafer (MPW) fabrication process by University of Washington [7]. In this section, firstly, the MZI fabrication process was described. Next, key features of EBL was introduced. Lastly, a corner analysis of the MZI performances was presented to predict the circuit behavior in the presence of the widest (worst) case variations of a thickness and a width of the waveguides due to manufacturing variability.

4.1. MZI fabrication process

A 6-inch (150-mm) SOI wafer (prime grade, Soitec) was used as the substrate, featuring a 220-nm thick crystalline silicon on top of 3- μm thick thermally grown SiO_2 buried oxide (BOX) layer. The substrate was solvent-rinsed and baked on a hot plate for dehydration. The SOI wafer was diced into 25 mm \times 25 mm dies. Subsequently, hydrogen silsesquioxane (HSQ, Dow-Corning XP-1541-006), a high-resolution negative-tone e-beam resist, was spin-coated onto the die at 4000 rpm, followed by baking on a hot plate at 80 $^\circ\text{C}$ for four minutes. The device layout design (GDSII) was converted to the EBL mask data for EBL by software of Beamer (GenlySys). The MZI device patterns were written on the resist using an electron beam (e-beam) lithography system (JEOL JBX-6300FS [8], JEOL Ltd.) operated at an acceleration energy of 100 keV, a beam current of 8 nA, a shot pitch of 6 nm, and exposure field size of 500 μm . An exposure dose was set to 2800 $\mu\text{C}/\text{cm}^2$. Next, the resist was developed by immersing the sample in 25% tetramethylammonium hydroxide (TMAH) for 4 minutes. The die was then rinsed with flowing deionized water (DI water) for 60 seconds and isopropanol (IPA) for 10 seconds, followed by nitrogen blow-drying. The exposed silicon areas, i.e., regions unexposed to e-beam, were etched using inductively coupled plasma reactive-ion etching (ICP-RIE) using Oxford Plasmalab System 100 (Oxford Instruments). The die was mounted on a 100-mm silicon carrier wafer using perfluoropolyether vacuum oil. The ICP-RIE process was carried out with a chlorine gas flow of 20 sccm, a chamber pressure of 12 mT, an ICP power of 800 W, a bias power of 40 W, and a platen temperature of 20 $^\circ\text{C}$, resulting in a bias voltage of 185 V. Lastly, the 2- μm thick SiO_2 cladding was deposited by plasma-enhanced chemical vapor deposition (PECVD, Oxford Plasmalab 100) with a silane (SiH_4) at 13 sccm, nitrous oxide (N_2O) at 1000 sccm, and high-purity nitrogen (N_2) at 500 sccm, under a chamber pressure of 1400 mT. PECVD process was performed with a high-frequency RF power of 120 W at 350 $^\circ\text{C}$.

4.2. Features of EBL

EBL is a direct-write technique (maskless lithography method) using a focused beam of electrons to directly transfer computer-designed patterns on to an electron-sensitive resist on a wafer, particularly for manufacturing nano-scale structures. Comparing to photolithography, EBL does not require photomasks (reticles) to fabricate, shortening lead time and lowering a cost to test new patterns. The feature offers greater flexibility for rapid prototyping, enabling the design of new components, testing novel concepts, validating numerical models, and evaluation of multiple design parameter variations within a single chip. A beam of electrons is generated electron gun, then focused and directed by an electromagnetic lens to strike specific locations on a resist. A beam of electrons can be focused to an area smaller than 3 nm, enabling a minimum feature size of 60 nm with a standard-thickness resist and as small as 10 nm with a thinner resist. The main disadvantage of EBL is, that EBL is a serial process, meaning the writing time is roughly proportional to the amount of area being exposed. Proximity correction has improved pattern fidelity by mitigating the proximity effect, which caused by backscattering of high-energy electrons from a silicon substrate to a resist on top, which leads to a background exposure in the vicinity of the patterns. The proximity correction is achieved by adjusting the electron exposure dose at each location, which is controlled by varying the dwell of the beam over different regions.

4.3. Corner analysis for MZIs

We employed a corner analysis to have a range of expected MZI performance variations due to manufacturing variability. In this report, the corner analysis was conducted under the assumption that material properties and waveguide path length variations were reasonably negligible, and only variations in waveguide thickness and width were considered. The thickness of the strip waveguide and its variation were determined by the Si wafer. The design target (T_m) was 220 nm, with a standard deviation (σ_T) of 3.9 nm, corresponding to 23.4 nm for a $6\sigma_T$. A thickness of 219.2 nm was taken as the mean value, resulting in the minimum (T_{\min}) and maximum (T_{\max}) values of 215.3 nm and 223.1 nm, respectively. Assuming a normal distribution, approx. 68% of the thickness values across the wafer fall within this range. In terms of the strip waveguide width, the total variation was influenced by both the inherent width variation and the presence of sloped sidewall, with typically 82 $^\circ$ sidewall angle. The strip waveguides were assumed substantial trapezoidal shape cross-section, instead of the ideal vertical sidewall profiles due to the etching process. Based on the empirical rules in this system, the design target (W_m), minimum (W_{\min}) and maximum (W_{\max}) values were set to 500 nm, 470 nm, and 510 nm, respectively. The corner

analysis was designed to examine the worst cases, i.e., four corner points, and the nominal design. Specifically, A set of (T_{\min}, W_{\min}) , (T_{\min}, W_{\max}) , (T_{\max}, W_{\min}) , (T_{\max}, W_{\max}) , and (T_m, W_m) were studied. Firstly, light propagation in the given set of designs was simulated using Lumerical MODE over a wavelength range from 1500 nm to 1600 nm. The effective and group index dispersions were computed using the simulations. The effective and group indices as functions of wavelength are plotted in Fig. 10. Subsequently, the effective index dispersions were fitted to the waveguide compact model (eq. (32)), calculating the effective and group indices, and group velocity dispersion at a wavelength of 1550 nm, as summarized in Table 2. The effective indices and group indices fell within ranges from 2.372 to 2.474 and from 4.179 and 4.260, respectively.

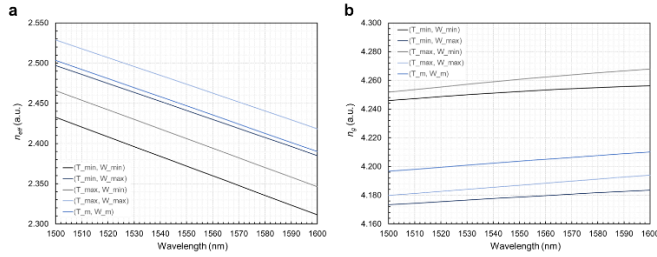


Fig. 10| Simulated (a) effective index and (b) group index dispersion.

Table 2| Fitting results of waveguide compact model in corner analysis.

Design ID	n_{eff} (a.u.)	n_g (a.u.)	D (ps/nm/km)
(T_{\min}, W_{\min})	2.372	4.252	351.2
(T_{\min}, W_{\max})	2.441	4.179	343.8
(T_{\max}, W_{\min})	2.406	4.260	547.9
(T_{\max}, W_{\max})	2.474	4.187	478.9
(T_m, W_m)	2.443	4.197	409.9

The obtained effective indices were used as inputs to compute the expected transfer functions based on eq. (19). Fig. 11 exhibits the transfer functions of MZI D1 as a representative example. The use of different effective indices resulted in shifts in the positions of the peaks and dips. Specifically, the peaks near a wavelength of 1550 nm, which was the central wavelength, were shifted within the range of 1546 nm and 1552 nm. The peaks for D1, D2, D3, D5 and D9 and the dips for D4, D6, D7, and D8 near a wavelength of 1550 nm were important in this report. Therefore, the nominal, minimum, and maximum values of the spectral features were summarized in Table 3. The FSR was also extracted from the transfer functions near a wavelength of 1550 nm. The nominal, minimum, and maximum values were depicted in Table 3. Provided that the assumptions in

this section are reasonable, the experimental results such as shifts of spectral peaks or dips, the group indices, and the FSR near a wavelength of 1550 nm are expected to fall within these predicted ranges.

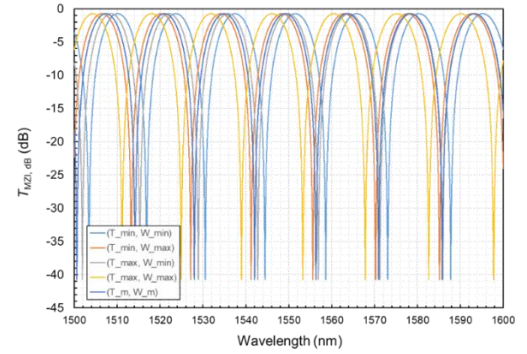


Fig. 11| Transfer functions of MZI D1 in corner analysis

Table 3| Expected range of peaks/dips shift and FSR by a corner analysis.

Device nr.	Peaks/Dips ^a (nm)			FSR (nm)		
	Nom.	Min.	Max.	Nom.	Min.	Max.
D1, D9	1549	1546	1552	14.45	14.24	14.50
D2	1549	1548	1553	7.19	7.09	7.25
D3, D5	1549	1548	1552	4.79	4.72	4.81
D4	1549	1548	1555	9.60	9.50	9.65
D6	1549	1545	1549	11.29	11.08	11.33
D7	1549	1548	1550	3.74	3.69	3.76
D8	1549	1549	1551	2.24	2.21	2.26

^a For the D1, D2, D3, D5, and D9, the nominal, minimal, and maximum values of a peak near a wavelength of 1550 nm. For the D4, D6, D7, and D8, the nominal, minimal, and maximum values of a dip near a wavelength of 1550 nm.

V. EXPERIMENTAL DATA

To characterize the MZI devices, a custom-built automated test setup^[9, 13] with automated control software written in Python was used^[10]. An Agilent 81600B tunable laser was used as the input source and Agilent 81635A optical power sensors as the output detectors. The wavelength was swept from 1500 to 1580 nm in 10 pm steps. A polarization maintaining (PM) fiber was used to maintain the polarization state of the light, to couple the TE polarization into the grating couplers^[11]. A 90° rotation was used to inject light into the TM grating couplers^[11]. A polarization maintaining fiber array was used to couple light in/out of the chip^[12].

The measured power transfer functions are visualized in Fig. 12a-c. MZI D1 was non-functional and as a result, the evaluation of manufacturing variability across the chiplet by comparing D1 with D9 was discontinued. All transfer functions, except for the one in D1, exhibited a sinusoidal oscillation and concave-down curves spectral response with respect to wavelength.

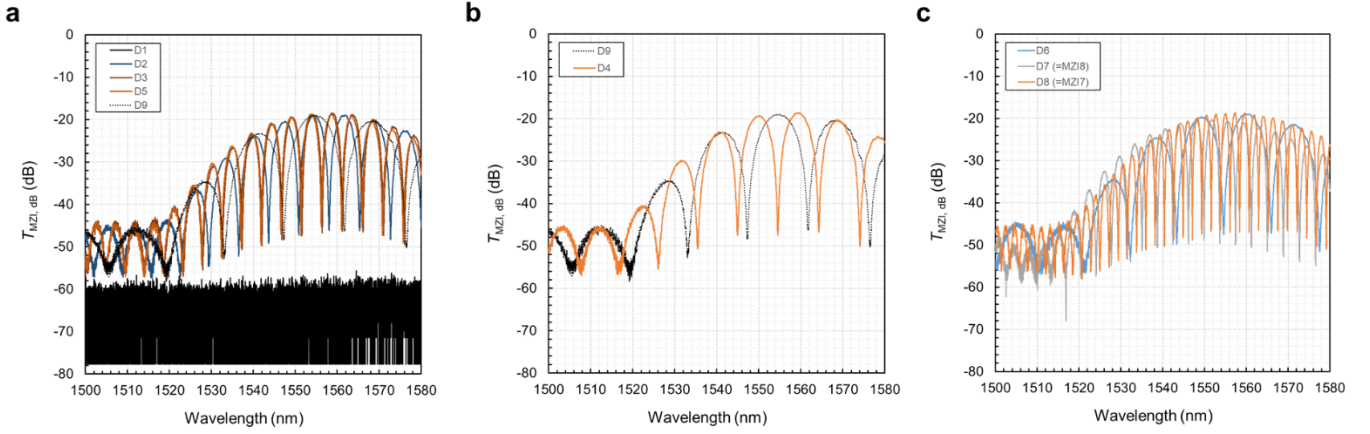


Fig. 12| Measured transfer functions of designed MZIs. **a**, transfer functions of D1, D2, D3, D5 and D9 in a range of wavelength from 1500 to 1580 nm, resulting in constructive interference near a wavelength of 1554 nm. **b**, transfer functions of D1, and D4 in the same range of wavelength. **c**, transfer functions of D6, D7 and D8 in the same range of wavelength, constructing destructive interference (dips) near a wavelength of 1554 nm.

The concave down curves were attributed to the wavelength-selective coupling efficiency of the two grating couplers in each MZI.

The maximum transmittance of each MZI ranged approximately from -19.0 dB to -18.7 dB within the wavelength range of 1550 nm to 1565 nm. For D9, D2, D3, and D5, these MZIs exhibited a peak near the wavelength of 1554 nm with different FSRs. In contrast, D4, D6, D7, and D8 demonstrated a dip near the same wavelength with different FSRs. As mentioned earlier, the target wavelength for constructive and destructive interferences in the designs were 1550 nm. Consequently, the constant peak or dip shifts of approx. 4nm were observed. This shift is not explainable by the corner analysis. The consistent shifts across the chiplet suggests either systematic variations or process drifts might affect every MZI. By taking into account the shifts, the results intuitively were consistent with the design concepts of the MZIs described in the “MODEL AND SIMULATION” section. By comparing D9 and D4, the constructive interference peak near the wavelength of 1554 nm observed in D9 approximately coincided the destructive interference dip near the same wavelength in D4. The result confirmed the design concept where, when an optical path length mismatch increases by a factor of 1.5, a constructive interference at the target wavelength shifts to destructive interference. Furthermore, a comparing D3 and D5, which had the identical optical path length mismatch but different number of waveguides in the path root, revealed that the number of waveguide bends within the limited range did not result in a difference in the transfer function of the MZIs.

VI. ANALYSIS

In the following section, the experimental results were analyzed, extracting key figures of merit of the MZIs. They are compared with the models and simulations and the corner analysis. Fig. 13. shows the sequential results obtained by

following the data analysis procedure using MZI D9 as a representative example. Firstly, the measured transfer functions were fitted to a fourth-order polynomial to remove the concave-down baseline caused by the finite bandwidth of the grating couplers, thereby flattening the spectra, shown in Fig. 13a. Subsequently, the flatten spectra were matched an interferometer model to extract the waveguide parameters. Starting eq. (17), when the propagation constants for both arms are identical, the equation can be rewritten as follow.

$$T_{MZI} = \frac{e^{-\alpha L}}{4} \left| 1 + \exp \left(-i\beta\Delta L - \frac{\alpha}{2}\Delta L \right) \right|^2 \quad (40)$$

where L is the unified optical path length, ΔL is an optical path length mismatch, $\beta (= \beta_1 = \beta_2)$ is a unified phase constant, and $\alpha (= 2\alpha_1 = 2\alpha_2)$ is an absorption coefficient (waveguide loss). Note that α_1 and α_2 are an attenuation constant. Based on eq. (40), the curve fitting function for the MZI transfer function can be written in the following equation.

$$F = 10 \log_{10} \left(\frac{1}{4} \left| 1 + \exp \left(-i\beta\Delta L - \frac{\alpha}{2}\Delta L \right) \right|^2 \right) + b \quad (41)$$

Where b (dB) is the excess insertion loss. Here, β is a function of an effective index as a function of wavelength according to eq.(6). Hence, β can be controlled by the unknown factors in eq. (32). These unknown factors, specifically n_1 , n_2 , and n_3 are fitting parameters used in the curve fitting process. The curve fitting was carried out using the least squares method, where the difference between the measured data and the transfer function model was minimized by adjusting the fitting parameters. Specifically, a non-linear fitting algorithm was employed for the curve fitting. The curve fitting requires reasonable initial parameter values to ensure that the algorithm can converge to a solution.

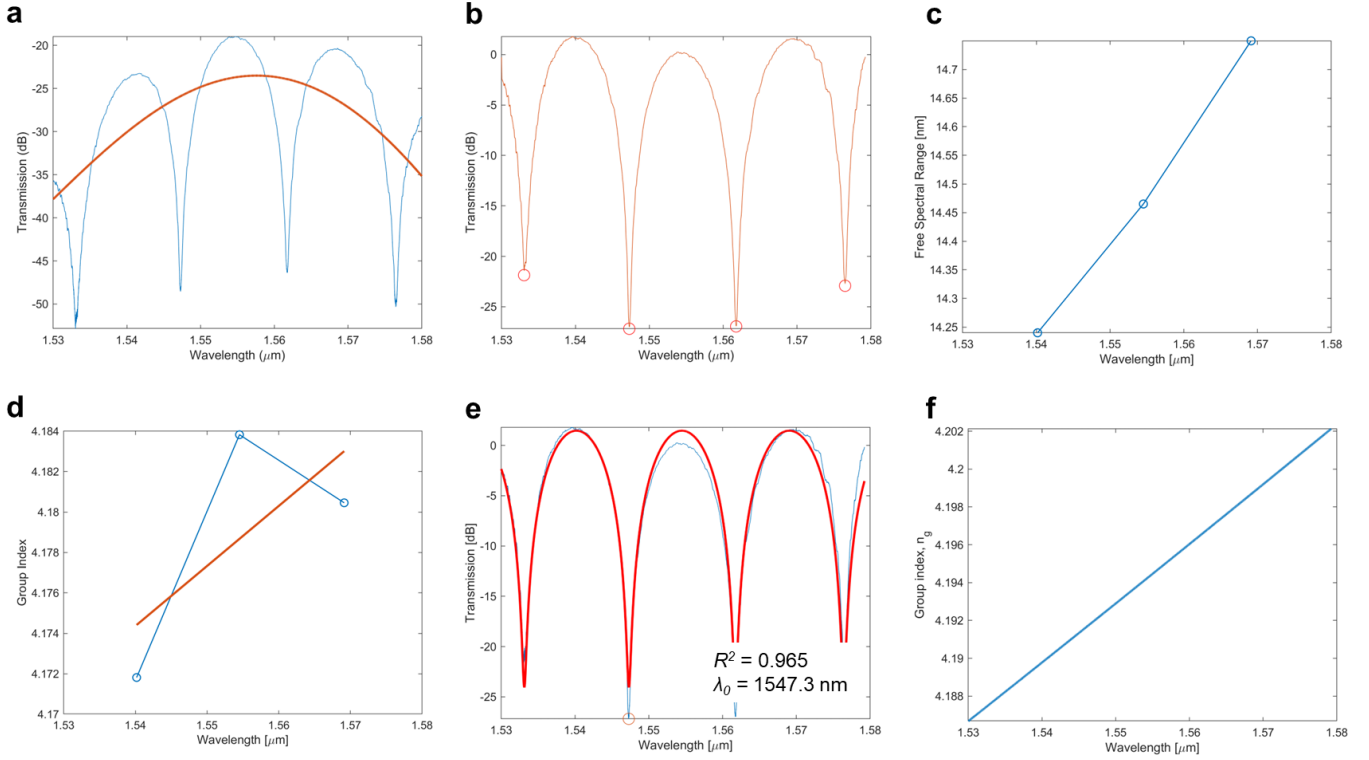


Fig. 13| Data analysis procedure for MZI transfer function using MZI D9 experimental data. **a**, Baseline correction of the measured transfer function (blue line) by fitting it to a fourth-order polynomial (red line). **b**, Identification of peaks (dips) in the baseline-corrected transfer function (orange line). The identified dip positions are marked with open red circles. **c**, FSR profile (open blue circles) extracted from peak (dip) identification. **d**, Group index profile (open blue circles) extracted from peak (dip) identification. **e**, Curve fitting function (red line) for the baseline corrected transfer function. The dip at the central wavelength used to align the curve fitting function to the experimental data is marked with an open red circle. **f**, Resulting group index dispersion derived by the data analysis.

To address this point, a peak-finding method was employed in this report. The robust method allowed to determine the suitable initial parameters numerically. The curve fitting process is detailed step by step in the following section. We start from the initial parameter determination. Firstly, the measured transfer function was smoothed using a moving average filter. Dips (minima) in the smoothed spectrum were identified, shown in Fig. 13b, as they can be more precisely located than the peaks due to their sharper nature on the decibel scale. From the spacing of dips in the baseline-corrected transfer function, the FSR profile with respect to the wavelength was calculated using eq. (21), plotted in Fig. 13c. The obtained FSR profile was then substituted into eq. (28), deriving the group index dispersion curve under the given optical path length mismatch ΔL . The average group index $n_{g,ave}$ across the wavelength was computed from the group index dispersion with values smaller than 3 or greater than 5 removed. Next, the target dip near the central wavelength λ_0 used for fitting the transfer function model was selected. In case of MZI D9, it was located at 1547.3 nm. Since a dip in the transfer function model corresponds to a destructive interference, the following conditions must be satisfied according to eq. (19).

$$\cos\left(\frac{2\pi n_{eff} \Delta L}{\lambda}\right) = -1 \quad (42)$$

$$\frac{2\pi n_{eff}}{\lambda} \Delta L = (2N + 1)\pi \quad (43)$$

$$N = \text{Round}\left(\frac{n_{eff} \Delta L}{\lambda} - \frac{1}{2}\right) \quad (44)$$

where N must be an integer. Here, the initial effective index $n_{eff,int}$ was set to 2.443 based to eq. (37) and λ_0 was used to derive the initial value of n_1 using the following equation in conjunction with eq. (43).

$$\begin{aligned} n_1 &= \frac{\lambda_0}{2\Delta L} (2N + 1) \\ &= \frac{\lambda_0}{2\Delta L} \left(2 \cdot \text{Round}\left(\frac{n_{eff,int} \Delta L}{\lambda} - \frac{1}{2}\right) + 1 \right) \end{aligned} \quad (45)$$

Next, the initial value of n_2 was calculated using the obtained n_1 by converting eq. (34) to the following equation.

$$n_2 = \frac{n_1 - n_{g,ave}}{\lambda_0} \quad (46)$$

Lastly, the initial value of n_3 was derived. Eq. (35) is transformed into the following expression, from which it can be understood that the value of n_3 can be determined once the slope of the group index with respect to wavelength is known.

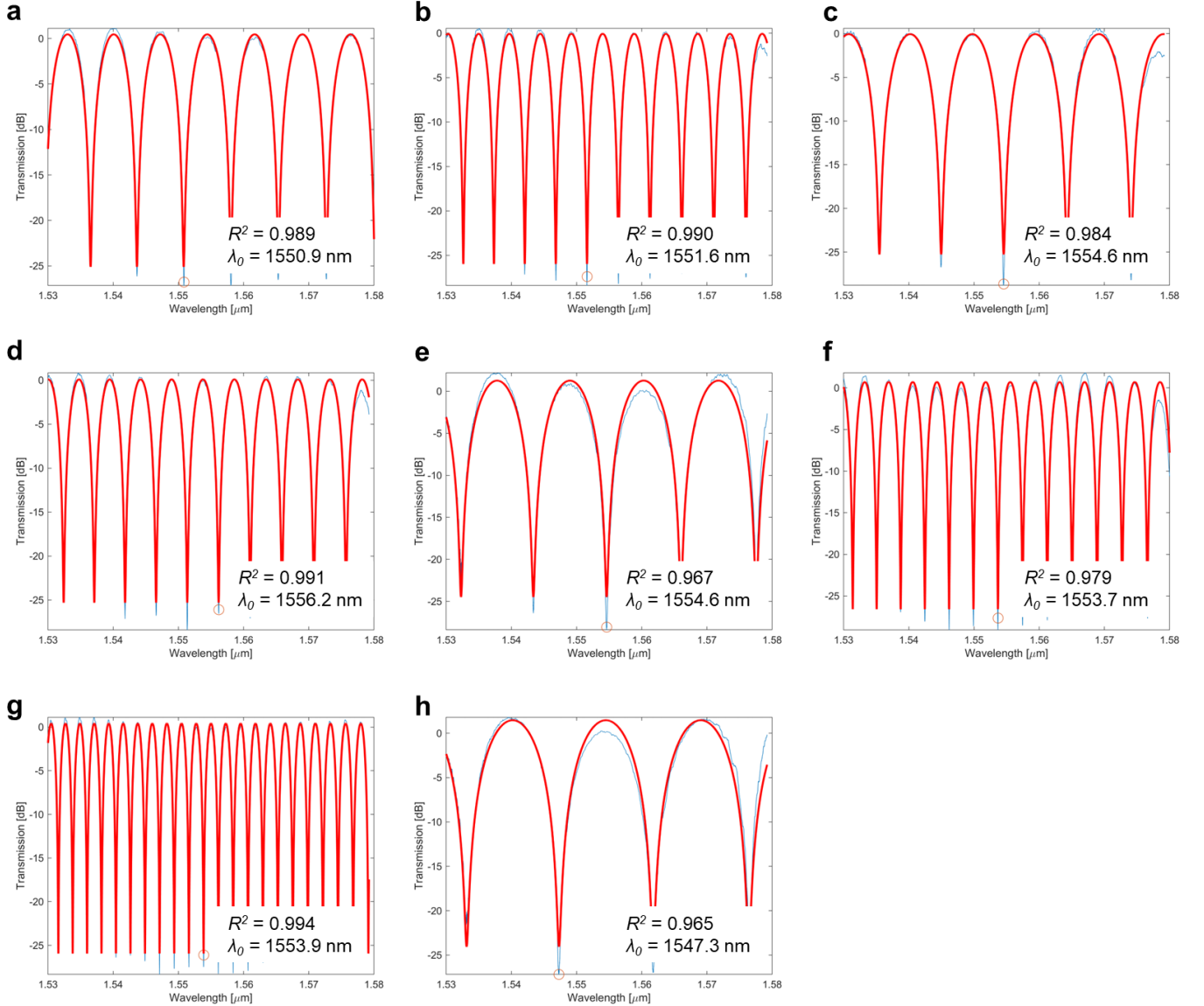


Fig. 14| Curve fitting functions for all functional MZIs. The baseline corrected transfer functions (red lines) and the fitted curve functions (blue line) for **a**, D2, **b**, D3, **c**, D4, **d**, D5, **e**, D6, **f**, D7 (=MZI8), **g**, D8 (=MZI7), and **h**, D9. The dip at the central wavelength used to align the curve fitting function to the experimental data is marked with an open red circle. R^2 represents the coefficient of determination of the curve fittings. λ_0 indicates the central wavelength.

$$n_3 = -\frac{1}{2\lambda_0} \frac{dn_g}{d\lambda} \quad (47)$$

The obtained group index dispersion was fitted with a linear function (Fig. 13d). The initial value of n_3 were derived in accordance to eq. (47) using the slot. The initial fitting parameters were now rationally determined. In the next step, the curve fitting using eq. (41) was applied to the processed experimental data. The parameters α and b were treated as constants and set to $10^{-3} \mu\text{m}^{-1}$ and 0, respectively. The fitting result is illustrated in Fig. 13e. Thereafter, the converged parameters n_1 , n_2 , and n_3 were used to compute the effective index, group index, group velocity dispersion, and FSR at the selected central wavelength λ_0 by employing eqs. (33), (34), (35), and (28), respectively. Additionally, the

group index dispersion across the wavelength range was determined using eq. (32) in conjunction with the following equation.

$$n_g = n_{eff}(\lambda) - \lambda \frac{dn_{eff}(\lambda)}{d\lambda} \quad (48)$$

Fig. 13f shows the resulting group index dispersion. The described data processing applied to all experimental data for the functional MZIs, presenting in Fig. 14. The curve fitting was successfully performed and closely matched the experimental spectrums, as evidenced by the coefficient of determination R^2 exceeding 0.965 for all MZIs. The key figures of merit for MZIs, including the effective index, group index, group velocity dispersion and free spectral range were extracted using the introduced data analytical procedure, and are summarized in Fig. 15 and Table 4.

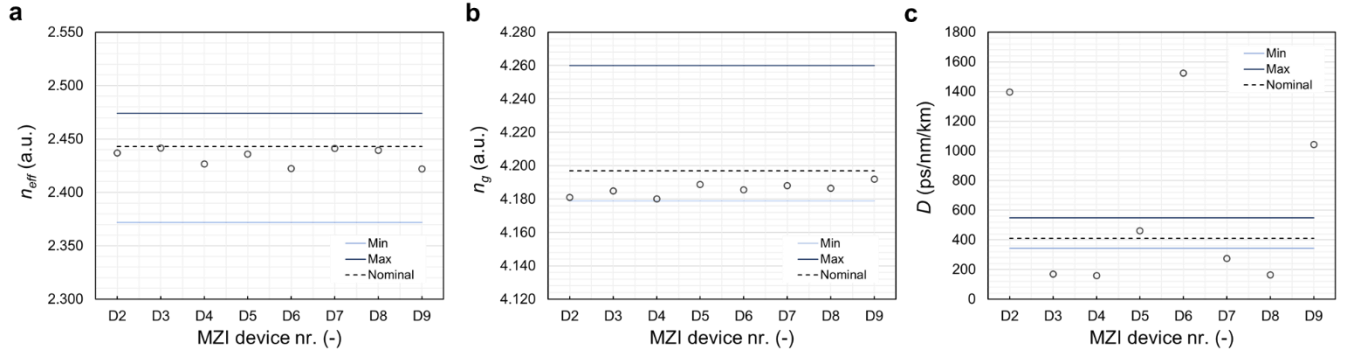


Fig. 15| Assessment using corner analysis. **a**, Effective indices (open black circles) derived from the data analysis for all MZIs compared with the range predicted by the corner analysis. **b**, Group indices (open black circles) derived from the data analysis for all MZIs compared with the range predicted by the corner analysis. **c**, Group velocity dispersion (open black circles) derived from the data analysis for all MZIs compared with the range predicted by the corner analysis. The nominal, minimum and maximum values of each waveguide parameters predicted by the corner analysis are overlaid as a black dotted line, light blue line, and dark blue line, respectively.

Comparing with the corner analysis, the resulting effective indices, and group indices were complied with the range for each given by the corner analysis. However, group velocity dispersions were out of the range predicted by the corner analysis. The calculated FSR near the central wavelength are presented in Table 4. As designed, the FSR of D2 and D3 were approx. half and one-third of that of D9, respectively. Additionally, the FSR of D7 and D8 were approx. one-third and one-fifth of that of D6, respectively. Comparing with the results in the corner analysis shown in Table 3, the resulting FSR coincided the FSR range predicted by the corner analysis. These results verified the design concepts, and the physical numerical models employed in this report, particularly, in term of investigating the effect of the path length mismatch in the imbalanced MZIs.

Table 4| Resulting key figures of merit of measured MZIs.

Device nr.	n_{eff} (a.u.)	n_g (a.u.)	D (ps/nm/km)	FSR (nm)
D2	2.437	4.181	1396.2	7.20
D3	2.442	4.185	168.1	4.80
D4	2.427	4.180	159.7	9.65
D5	2.436	4.189	460.3	4.83
D6	2.422	4.186	1524.9	11.32
D7 (=MZI8)	2.441	4.188	274.6	3.77
D8 (=MZI8)	2.440	4.186	165.0	2.26
D9	2.442	4.192	1042.0	14.30

VII. CONCLUSION

The effects of path length mismatch and optical path root structures on the performance of MZIs were investigated. The experimental transfer function results closely matched the simulations based on the introduced MZI transfer function model. Hence, it was verified that the design concept of controlling the positions of constructive and destructive interference, as well as the FSR by varying the

optical path length mismatch. It provides robust design rules for MZIs. Additionally, it was verified that the number of waveguide bends, up to 10, with a radius of 5 μm in the strip waveguide operating in quasi-TE mode does not impact the power transmittance efficiency of MZIs. This finding allows for reduction of a footprint of MZI devices while maintaining the same path length mismatch. The key figures of merit for MZIs including the effective index, group index, group velocity dispersion and FSR were extracted by curve-fitting the experimental data to the transfer function model. These values fell within the range predicted by the corner analysis, except for the group velocity dispersion. The result enables designers to incorporate a manufacturing variability into design rules, enhancing robustness during the design phase. Lastly, all measured transfer functions exhibited a shift of approx. 4 nm upwards in either peaks or dips, compared to the simulation in the design. The consistent nature of shifts across the chiplet suggests the presence of either systematic variations or process drifts affecting all MZIs. Further work is required to understand a root-cause analysis of the origin of the shifts.

ACKNOWLEDGMENT

I acknowledge the edX UBCx Phot1x Silicon Photonics Design, Fabrication and Data Analysis course, which is supported by the Natural Sciences and Engineering Research Council of Canada (NSERC) Silicon Electronic-Photonic Integrated Circuits (SiEPIC) Program. The devices were fabricated by Richard Bojko at the University of Washington Washington Nanofabrication Facility, part of the National Science Foundation's National Nanotechnology Infrastructure Network (NNIN), and Cameron Horvath at Applied Nanotools, Inc. Omid Esmaeeli performed the measurements at The University of British Columbia. I acknowledge Lumerical Solutions, Inc., Mathworks, Mentor Graphics, Python, and KLayout for the design software.

REFERENCES

- [1] Chrostowski, L. & Hochberg, M. *Silicon Photonics Design* 4th edn, pp. 1-27 (Cambridge university press, 4th-Edition, 2020).
- [2] Butt, M. A. et al. Strategic Insights into Integrated Photonics: Core Concepts, Practical Deployments, and Future Outlook. *Appl. Sci.* **14**, 6365 (2024).
- [3] Chrostowski, L. & Hochberg, M. *Silicon Photonics Design* 4th edn, pp. 110-114 (Cambridge university press, 4th-Edition, 2020).
- [4] KLayout. <https://www.klayout.de/> (2025).
- [5] GitHub, SiEPIC EBeam PDK & Library, for SiEPIC-Tools and KLayout. https://github.com/SiEPIC/SiEPIC_EBeam_PDK (2025).
- [6] Chrostowski, L. & Hochberg, M. *Silicon Photonics Design* 4th edn, pp. 66-69 (Cambridge university press, 4th-Edition, 2020).
- [7] R. J. Bojko, J. Li, L. He, T. Baehr-Jones, M. Hochberg, and Y. Aida, "Electron beam lithography writing strategies for low loss, high confinement silicon optical waveguides," *J. Vacuum Sci. Technol. B* **29**, 06F309 (2011).
- [8] University of Washington, Nanofabrication Facility. <https://ebeam.mff.uw.edu/ebeamweb/> (2025)
- [9] Lukas Chrostowski, Michael Hochberg, chapter 12 in "Silicon Photonics Design: From Devices to Systems", Cambridge University Press, 2015.
- [10] <http://siepic.ubc.ca/probestation>, using Python code developed by Michael Caverley.
- [11] Yun Wang, Xu Wang, Jonas Flueckiger, Han Yun, Wei Shi, Richard Bojko, Nicolas A. F. Jaeger, Lukas Chrostowski, "Focusing sub-wavelength grating couplers with low back reflections for rapid prototyping of silicon photonic circuits", *Optics Express* Vol. **22**, Issue 17, pp. 20652-20662 (2014).
- [12] www.plconnections.com, PLC Connections, Columbus OH, USA.
- [13] <http://mapleleafphotonics.com>, Maple Leaf Photonics, Seattle WA, USA.